

A titanium surface with nano-ordered spikes and pores enhances human dermal fibroblastic extracellular matrix production and integration of collagen fibers

This content has been downloaded from IOPscience. Please scroll down to see the full text.

2016 Biomed. Mater. 11 015010

(<http://iopscience.iop.org/1748-605X/11/1/015010>)

View [the table of contents for this issue](#), or go to the [journal homepage](#) for more

Download details:

IP Address: 130.34.173.69

This content was downloaded on 02/02/2016 at 16:26

Please note that [terms and conditions apply](#).

# Biomedical Materials



## PAPER

# A titanium surface with nano-ordered spikes and pores enhances human dermal fibroblastic extracellular matrix production and integration of collagen fibers

RECEIVED  
7 September 2015

REVISED  
24 November 2015

ACCEPTED FOR PUBLICATION  
11 December 2015

PUBLISHED  
2 February 2016

Masahiro Yamada<sup>1,2</sup>, Eiji Kato<sup>1</sup>, Akiko Yamamoto<sup>3</sup> and Kaoru Sakurai<sup>1</sup>

<sup>1</sup> Department of Removable Prosthodontics and Gerodontology, Tokyo Dental College, Tokyo, Japan

<sup>2</sup> Division of Molecular and Regenerative Prosthodontics, Tohoku University Graduate School of Dentistry, Miyagi, Japan

<sup>3</sup> Biomaterials Group, Biomaterials Unit, Nano-Life Field, MANA, National Institute for Materials Science, Ibaraki, Japan

E-mail: [masahiro.yamada.a2@tohoku.ac.jp](mailto:masahiro.yamada.a2@tohoku.ac.jp) and [masayamada1020@gmail.com](mailto:masayamada1020@gmail.com)

**Keywords:** anisotropy, bone-anchored prosthesis, focal adhesion, isotropy, nano-technology, soft tissue integration, surface topography

## Abstract

The acquisition of substantial dermal sealing determines the prognosis of percutaneous titanium-based medical devices or prostheses. A nano-topographic titanium surface with ordered nano-spikes and pores has been shown to induce periodontal-like connective tissue attachment and activate gingival fibroblastic functions. This *in vitro* study aimed to determine whether an alkali-heat (AH) treatment-created nano-topographic titanium surface could enhance human dermal fibroblastic functions and binding strength to the deposited collagen on the titanium surface.

The surface topographies of commercially pure titanium machined discs exposed to two different AH treatments were evaluated. Human dermal fibroblastic cultures grown on the discs were evaluated in terms of cellular morphology, proliferation, extracellular matrix (ECM) and proinflammatory cytokine synthesis, and physicochemical binding strength of surface-deposited collagen.

An isotropically-patterned, shaggy nano-topography with a sponge-like inner network and numerous well-organized, anisotropically-patterned fine nano-spikes and pores were observed on each nano-topographic surface type via scanning electron microscopy. In contrast to the typical spindle-shaped cells on the machined surfaces, the isotropically- and anisotropically-patterned nano-topographic titanium surfaces had small circular/angular cells containing contractile ring-like structures and elongated, multi-shaped cells with a developed cytoskeletal network and multiple filopodia and lamellipodia, respectively. These nano-topographic surfaces enhanced dermal-related ECM synthesis at both the protein and gene levels, without proinflammatory cytokine synthesis or reduced proliferative activity. Deposited collagen fibers were included in these surfaces and sufficiently bound to the nano-topographies to resist the physical, enzymatic and chemical detachment treatments, in contrast to machined surfaces.

Well-organized, isotropically-/anisotropically-patterned, nano-topographic titanium surfaces with AH treatment-created nano-spikes and pores enhanced human dermal fibroblastic ECM synthesis and established sufficient mechanical integration between the surfaces and ECM to resist various detachment treatments used to experimentally mimic overloading and inflammation.

## 1. Introduction

Percutaneous implants/devices include silicone rubber-based continuous ambulatory peritoneal dialysis catheters, cardiac assist systems with metal protective sleeves, bone-anchored metal pedestals for anchoring external electrical sound processors, and titanium

implants used to support artificial eye/cochlear, limb or cranio-maxillofacial prostheses [1]. In the medical and dental fields, these mandatory devices are necessary for life-support and functional recovery because they percutaneously transfer mass, force or energy into the deep tissues. However, these devices are often associated with concerns regarding looseness and infection in the

peri-implant skin [2–4]. The percutaneous portions of these devices are covered in a protective metal sleeve, and the devices are frequently composed of titanium or an alloy. The epidermis and dermis attach to the implant surface at the skin-implant interface. Because of post-healing turnover, the peri-implant epidermis exhibits gradual downward growth along the implant surface; this results in sulcus formation around the implant. The sulcus provides a habitable environment and infectious pathway to pathogens. In addition, the skin-implant interface is frequently subjected to tearing forces caused by skin retraction from scar tissue around the implant, leading to increased risks of infection and implant loosening. Enhanced peri-implant skin sealing would effectively prevent both infection and implant loosening, and reinforcement of the dermal attachment on the implant surface is a crucial step in this process.

The dermis comprises three layers, the papillary, subpapillary and reticular layers, and accounts for the majority of skin tissue, with a thickness approximately 15–40 folds greater than that of the epidermis. The reticular layer, which contains dense connective tissue, accounts for the largest part of the dermis, and therefore determines the mechanical stability of skin tissues. Dermal connective tissue comprises collagen fibers composed of mostly type I and III collagens, elastic fibers composed of elastin and fibrillin, and grounded matrix components such as fibronectin. Dermal fibroblasts produce extracellular matrices (ECMs) of dermal connective tissue, and the expression levels of these components on percutaneous implants may determine the mechanical stability of peri-implant dermal tissue.

From the perspective of biological sealing at soft tissue interfaces, the periodontal tissue structure merits attention. Gingival connective tissue mechanically binds to the roots of teeth by inserting collagen fibers into cementum on the roots as Sharpey's fibers. A nano-topographic approach can establish the ultrastructure necessary for cellular infiltration into the porous internal microstructure [5] and to enhance cellular differentiation [6–8]. Recently, a nano-topographic titanium surface featuring nano-edges, spikes and crevasses created using alkali-heat (AH) treatment was shown to promote the inclusion of gingival connective tissue fibers into the surface [9]. This titanium surface strongly bound collagen deposited on the surface through the inclusion of collagen fibers into the AH-created crevasses to a level sufficient to resist experimental overloading and inflammatory conditions. The inclusion of gingival connective tissue into the titanium surface was confirmed using a rabbit maxilla implantation model [9]. In addition, the nano-edges and spikes on the nano-topographic surface enhanced gingival fibroblastic cellular adhesion and collagen synthesis in the same manner as other nano-topographic substrates with nanometer-sized protrusions by influencing cellular attachment, adhesion, subsequent cellular proliferation and ECM production [10–19].

Generally, cellular behavior with respect to a substrate's nano-topography varies according to cell type [20, 21]. Gingival fibroblasts are potentially different from dermal fibroblasts in terms of phenotypic factors, such as cell adhesion molecules [22, 23]. Recently, it was suggested that during wound healing, dermal fibroblasts determine the direction of migration by sensing the nano-topography gradients of the underlying matrix [24]. This finding supported the idea that dermal fibroblasts are more sensitive than endothelial and smooth muscle cells to substrate's nano-topography, which leads to a modulation of their function [20]. Therefore, it was hypothesized that AH-treated nano-topographic titanium surfaces enhanced dermal fibroblasts beyond the differences in cell type, and thus strongly interlocked with dermal collagen fibers. The purpose of this *in vitro* study was to determine whether these nano-topographic titanium surfaces could enhance the functions of human dermal fibroblasts and binding strength to surface-deposited collagen under various detachment treatments.

## 2. Materials and methods

### 2.1. Sample preparation

Commercially pure grade 2 machined titanium discs (20 mm diameter and 1 mm thickness) used as a culture substrate and grade 1 titanium film (10 mm<sup>2</sup> area and 0.1 mm thickness) were purchased (Nishimura Co., Ltd., Fukui, Japan). The titanium samples were washed by ultrasonication in a series of ethanol and Milli-Q water after acetone cleaning. Two types of nano-topographical titanium surfaces were then prepared according to two previously reported AH treatment protocols [9]. Briefly, the cleaned machined discs were boiled in a 5 mol l<sup>-1</sup> sodium hydroxide solution at 60 °C for 24 h. After washing in Milli-Q water and air-drying, the discs were heated in a furnace with a steadily increasing temperature (5 °C increase/min) and sintered at 600 °C for 1 h. After sintering, the discs were naturally cooled. This protocol is abbreviated as a 5 M AH treatment. In the other protocol, abbreviated as a 10 M AH treatment, the discs were boiled in a 10 mol l<sup>-1</sup> sodium hydroxide solution at 90 °C for 24 h, followed by the previously described sintering process. All prepared samples were rinsed under ultrasonication in Milli-Q water for 10 min and stored in ambient conditions in the dark for 4 weeks prior to use. All discs and films used in culture experiments were placed on 12-well culture-grade polystyrene plates.

### 2.2. Surface characterization

The surface topographies of the sample discs were evaluated via scanning electron microscopy (SEM; XL30; Philips, Eindhoven, Netherlands) and the surface roughness at the micron-level was measured using a 3D-measuring laser microscope (LEXT OLS4000; Olympus, Tokyo, Japan) with a cut-off value of 8 μm and measurement length of 120 μm. Morphological

features of the AH-treated layers were determined by SEM observation and image analysis of cross-sectional specimens of AH-treated titanium films prepared by cutting the film with stainless steel scissors; images were processed using ImageJ software (National Institutes of Health, Bethesda, MD, USA). Top-to-top distances of the convex superior nano-topographical areas were measured. The chemical properties of AH-treated surfaces were evaluated via elemental analysis of the titanium surface using an electron probe microanalyzer (EPMA; JXA-8200; JEOL Ltd., Tokyo, Japan) before and after a 7 d immersion in culture media.

### 2.3. Human dermal fibroblastic culture

Normal adult human dermal fibroblasts were purchased (NHDF-Ad, Lonza, Basel, Switzerland) and plated in 100 mm plastic tissue culture dishes with Dulbecco's modified Eagle's medium supplemented with 10% fetal bovine serum and antibiotic-antimycotic solution, containing 100 U ml<sup>-1</sup> penicillin G sodium, 100 µg ml<sup>-1</sup> streptomycin sulfate and 250 ng ml<sup>-1</sup> amphotericin B in a humidified atmosphere of 95% air and 5% CO<sub>2</sub> at 37 °C. The cells were passaged for a second time when 80% confluency was achieved. After the second passage, the cells were detached using 0.25% Trypsin-1 mM EDTA-4Na in Dulbecco's modified phosphate buffered saline (D-PBS) and seeded directly onto the titanium discs or films with machined and 5 or 10 M AH-treated surfaces at  $3.0 \times 10^4$  cells cm<sup>-2</sup>. The medium was renewed every 3 d.

### 2.4. Cellular morphology and attachment

For the immunofluorescent analysis, day 1 cultures of dermal fibroblasts on discs with machined or 5 or 10 M AH-treated surfaces were fixed in 10% neutral buffered formalin for 30 min. The cells were then treated with 0.1% Triton-X for 5 min and subsequently stained with 2% rhodamine phalloidin (Molecular Probes, Eugene, OR, USA) in phosphate-buffered saline (PBS) and 4',6-diamidino-2-phenylindole (DAPI; Vector Laboratories, Burlingame, CA, USA) in a mounting agent. The cell morphologies and cytoskeletal arrangements were observed under a fluorescent photomicroscope (Axiophoto2; Carl Zeiss Co., Ltd., Jena, Germany). Cell morphometry was analyzed using ImageJ software. For SEM analysis, day 1 cultures were fixed with 2.5% glutaraldehyde prior to vapor-deposited with 1% osmium tetroxide. The samples were subsequently subjected to critical point drying and gold coating.

### 2.5. Cellular attachment and proliferation

Cell viability in day 1 and 7 cultures grown on discs with machined or 5 or 10 M AH-treated surfaces were evaluated via tetrazolium salt-based colorimetry (WST-1; Roche Diagnostics, Tokyo, Japan). Each culture was incubated for 4 h at 37 °C in 1 ml of fresh culture media containing 100 µl of WST-1 reagent. The amount of formazan produced by viable cells was

measured colorimetrically at 420 nm using a microplate reader. The cell proliferative activity was measured by bromodeoxyuridine (BrdU) incorporation during DNA synthesis. On day 4 of the titanium surface cultures, a 100 µl portion of 100 mM BrdU solution (100 ml; Roche Diagnostics, Tokyo, Japan) was added to each of the culture wells, followed by a 10 h incubation period. The DNA was subsequently denatured and the cultures were incubated with a peroxidase-conjugated anti-BrdU antibody for 90 min and exposed to tetramethylbenzidine for color development. The absorbance at 370 nm was measured using an enzyme-linked immunosorbent assay reader.

### 2.6. Collagen production

On day 28, the disc cultures were subjected to a Sirius red-based colorimetric assay to quantify collagen production. Cultures on different discs were washed with pre-warmed PBS (37 °C) for 1 min and fixed with Bouin's fluid for 1 h at room temperature. The cultures were washed with Milli-Q water and treated with 0.2% aqueous phosphomolybdic acid for 1 min. The cultures were washed again with Milli-Q water and stained with Sirius red dye (C.I. No. 35780, Pfaltz and Bauer, Stamford, CT, USA) dissolved in saturated aqueous picric acid (pH 2.0) at a concentration of 1 mg ml<sup>-1</sup> for 90 min with mild shaking. The cultures were washed with 0.01 N hydrochloric acid for 2 min to remove all non-bound dye. Next, 600 µl of 0.1 N sodium hydroxide was added to dissolve the stain, and the samples were placed on a microplate shaker for 30 min at room temperature. The absorbance of the solutions at 550 nm was measured with a spectrophotometer; 0.1 N sodium hydroxide was used as a blank. The absorbance value of each culture was subtracted from the value of the corresponding disc without cells.

### 2.7. Gene expression analysis

Gene expression on day 14 was analyzed via reverse-transcriptase polymerase chain reaction (PCR). Total RNA was extracted from the cell cultures using TRIzol (Invitrogen, Carlsbad, CA, USA) and a purification column (RNeasy, Qiagen, Valencia, CA, USA). Following DNase I treatment, 0.5 mg of total RNA was reverse transcribed using MMLV reverse transcriptase (Clontech, Carlsbad, CA, USA) in the presence of oligo(dT) primers (Clontech). PCR was performed with Taq DNA polymerase (EX Taq; Takara Bio, Madison, WI, USA) to detect collagen I and III mRNA. The PCR products were separated on a 1.5% agarose gel and visualized by ethidium bromide staining. Band intensity was detected under UV light and normalized with reference to *GAPDH* mRNA. Gene expression analyses were performed three to five times, and representative data sets are presented after confirming consistency.

### 2.8. Cellular proinflammatory cytokine detection

The levels of proinflammatory cytokine synthesis in human dermal fibroblasts cultured on titanium discs

for 3 d were quantified using a multiplex cytokine immunoassay system (Veritas, Tokyo, Japan). The cells were washed twice with PBS and lysed in 200  $\mu$ l PBS by freeze/thawing. The lysates were incubated with beads coated with antibodies corresponding to various cytokines according to the manufacturer's instructions. The bead sizes and fluorescence levels were measured on a Luminex 200 system (Luminex Japan, Tokyo, Japan). Data were analyzed using a MasterPlex QT (Hitachi Solutions, Tokyo, Japan).

### 2.9. Analysis of ECM surface deposition method

To evaluate the ECM surface morphology, day 28 cultures grown on discs with machined or 5 or 10 M AH-treated surfaces were subjected to SEM observation after fixation with 2.5% glutaraldehyde and dehydration in a graded ethanol series (50–100%) and vapor-deposited with 1% osmium tetroxide. To determine the inclusion of deposited ECM into the nano-featured surface, day 28 cultures grown on titanium films with 5 or 10 M AH-treated surfaces were cut with stainless steel scissors after fixation. SEM was used to gain a bird's eye view of cross-sectional specimens of film containing superficial culture layers.

### 2.10. Collagen detachment assay

To evaluate the mechanical, enzymatic, and chemical strengths of the deposited collagen on titanium surfaces under overloading or inflammatory conditions, day 28 cultures on discs were subjected to various detachment treatments (e.g. ultrasonication or exposure to collagenase or hydrogen peroxide) [9]. The cultures were washed twice with PBS. Subsequently, cultures in PBS were placed on ultrasonic equipment (UT105, Sharp, Tokyo, Japan) at 100 W and 35 kHz for 1 min to simulate an overloading condition. To simulate an inflammatory condition, the remaining day 28 cultures were incubated at 37 °C in PBS containing 0.1 U ml<sup>-1</sup> collagenase (Roche Diagnostics) for 1 h or 0.3 mmol l<sup>-1</sup> hydrogen peroxide for 3 h, respectively. Subsequently, the cultures were stained with Sirius red, and absorbance was measured according to the above-described protocol. The absorbance value of each culture was subtracted from the value on the corresponding disc without cells. The percentage of remaining collagen was calculated as ((Sirius red absorbance of the culture after detachment treatment/absorbance of the corresponding duplicated day 28 culture without detachment treatment)  $\times$  100) (%). In addition, after collagenase treatment, some of the day 28 cultures were subjected to SEM observation to evaluate the morphology associated with the mode of detachment.

### 2.11. Statistical analysis

To determine the top-to-top nano-topographical distances, a total of 50 such intervals were measured on 20 000  $\times$  SEM images on two different cross-sectional samples of AH-treated titanium film. To assess the micro-roughness of the surface topography or the

chemical properties of the surfaces after immersion in culture media for 7 d, six different 2000  $\times$  or 1000  $\times$  spots were randomly selected on the titanium surface for laser microscopic or EPMA analysis. The mean value of the six spots was set as a representative value for each sample. Each measurement was repeated with five different discs per group ( $n = 5$ ). For all culture experiments involving quantitative assays except for cellular morphology, three independent cultures with different batches of cells were evaluated per group ( $n = 3$ ), and at least three replicates were included per experiment. To assess cellular morphometry, six single cells with typical morphological features were randomly selected from three different points on the titanium surface. The mean value of the six single cells was set as a representative value for each sample. Each experiment was repeated five times with different discs and cell batches per group ( $n = 5$ ). The Mann–Whitney U-test was used to examine differences between two groups. An analysis of variance was used to assess differences among multiple experimental groups and, when appropriate, Bonferroni multiple comparison testing was used. A  $p$ -value  $< 0.05$  was considered statistically significant.

## 3. Results

### 3.1. Nano-topographic titanium surface features without micron-level influence after AH-treatment

Macroscopic images (figure 1(A), top panels) revealed that the titanium surface color changed from metallic silver to yellow or marine blue after 5 or 10 M AH-treatment. SEM images (figure 1(A),  $\times 2000$ ) revealed that the 5 and 10 M AH-treated surfaces exhibited unidirectionally coasting waves at intervals of a few microns, suggestive of the topography of the machined substrate, which featured lined and wavy microgrooves. Higher magnification images (figure 1(A),  $\times 10\,000$  and  $\times 50\,000$ ) revealed that the 5 M AH-treated surface exhibited shaggy structures with multiple spikes and connection holes that progressed to a nanoscale sponge-like inner network, whereas the 10 M AH-treated surface contained numerous well-organized and dense nano-edges and spikes with multiple nano-sized crevasses and holes. The array of nano-spikes and pores on the 5 M AH-treated surface appeared to be isotropically-patterned, whereas the 10 M AH-treated surfaces contained ordered but anisotropically-patterned and random features. The top-to-top distances in the nano-spikes appeared smaller on the 10 M AH-treated surfaces than on the 5 M-treated surfaces.

3D laser microscopic isometric images (figure 1(B), top panels) demonstrated that the extent of micron-order roughness was similar among all types of surfaces, where a few micron-sized grooves were observed. The 5 MAH-treated surfaces exhibited the lowest values with respect to the 3D mean roughness ( $S_a$ ) and root mean square ( $R_{ms}$ ) but were comparable with the machined surface in terms of the 3D maximum height ( $S_z$ )

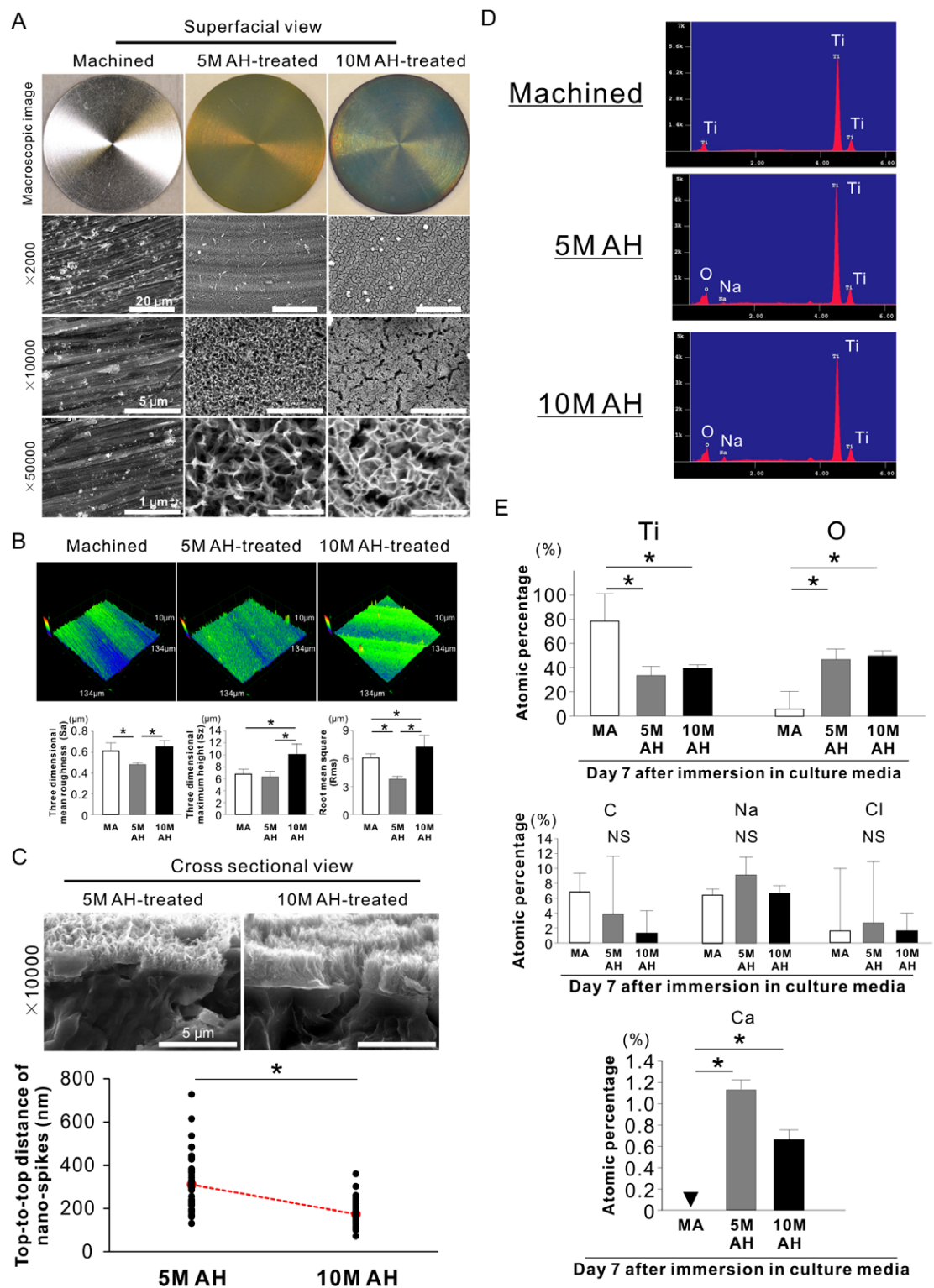


**Figure 1.** (A) Representative macroscopic and scanning electron microscope (SEM) images of titanium discs with machined and 5 and 10 M alkali-heat (AH)-treated surfaces. The bar scales in images are equal at the same magnification level. (B) Laser microscopic 3D images and quantitative measurements of three surface roughness parameters at micron-level on titanium discs with machined (MA) and 5 and 10 M AH-treated surfaces. (C) Representative SEM images and quantitative measurements from cross-sections of 5 and 10 M AH-treated surfaces on titanium films, showing the top-to-top distances of nano-spikes. Data are shown as dot plots with 50 dots per group; median values are indicated by the ends of the dashed lines. Electron probe microanalyzer elemental analysis of titanium discs with machined (MA) and 5 and 10 M AH-treated surfaces before (D) and after 7 d immersion in the culture media used in the present study (E). Data are shown as means  $\pm$  standard deviations ( $n = 5$ ). \* $p < 0.05$ , indicating a statistically significant difference between multiple experimental groups (Bonferroni) and differences between two groups (Mann-Whitney U test).

(figure 1(B), bottom histograms). The 10 MAH-treated surfaces exhibited the highest values in  $S_z$  and  $R_{ms}$  but did not differ from the machined surface in  $S_a$ . SEM observation of surface cross-sections demonstrated a uniform nano-shaggy structure on the 5 MAH-treated surface, whereas the 10 MAH-treated surface featured closely packed bunches of finer nano-edges and spikes with a monolithic-like structure towards the titanium substrate (figure 1(C), top images). The nanostructured superficial layers were approximately 600 and 900 nm thick on the 5 and 10 MAH-treated surfaces, respectively. The median nano-spike top-to-top distances were 303 and 160.5 nm on the 5 and 10 MAH-treated surfaces, respectively ( $p < 0.05$ , Mann–Whitney U-test; figure 1(C), bottom dot plot).

### 3.2. Chemical properties of the AH-treated titanium surface

In addition to titanium, sodium and oxygen were detected via EPMA on both the 5 and 10 MAH-treated surfaces, whereas only titanium was detected on the machined surface (figure 1(D)). Oxygen was the most common element on both AH-treated surfaces after immersion into culture media for 7 d, whereas titanium was most common on the machined surface ( $p < 0.05$ , Bonferroni; figure 1(E), left histogram). There were no significant differences in other detected elements, such as carbon, sodium and chloride (figure 1(E), mid histogram). However, calcium was detected only on the AH-treated surfaces, and the 5 MAH-treated surface had a 2-fold higher calcium level than the 10 MAH-treated surface ( $p < 0.05$ ; figure 1(E), right histogram).

### 3.3. Dermal fibroblastic attachment and morphology on the AH-treated titanium surfaces

Fluorescent microscopic images of DAPI and rhodamine stained samples (figure 2(A), upper images) demonstrated that although the day 1 human dermal fibroblastic cultures were comparable with respect to the nuclear numbers of attached cells, the surface types were associated with totally different cell shapes. On the machined surface, dermal fibroblasts exhibited unidirectionally elongated spindle shapes with relatively well-developed and unidirectional actin formation and lamellipodia (figure 2(A), left lower image). In contrast, cells grown on the 5 MAH-treated surface were small but featured an angular or circular shape, with spotty or circular actin accumulation inside and at the edge of the cells as contractile ring-like structures (figure 2(A), triangles and arrowheads in the mid-lower image). On the 10 MAH-treated surface, the cells exhibited rectangular, spindle, or oval shapes with moderate expansion (figure 2(A), right upper image) and developed a cytoskeletal network with multiple orientations, multiple filopodia-like projections (figure 2(A), arrow in right lower image), and actin accumulation at the concave edges (similar to lamellipodia) and within the cell (figure 2(A), triangles and arrowheads in the right lower image). Cells grown

on 5 MAH-treated surfaces had cell morphological parameter values (e.g. area, perimeter and Feret's diameter) that were less than 20% of those on the machined surface (figure 2(B),  $p < 0.05$ , Bonferroni). In contrast, the perimeter value of the 10 MAH-treated surface was comparable to that of the machined surface. Area and Feret's diameter were lower on the 10 MAH-treated surface than on the machined surface, but these differences represented approximately 30% reductions.

SEM observation of day 1 cultures revealed cellular morphological features similar to those observed under fluorescent microscopy (figure 2(C), upper images). The cell margins were unclear and appeared to incorporate into the nano-spikes and pores on both the 5 and 10 MAH-treated surfaces (figure 2(C), triangles in lower middle and right images), in contrast with the flat cellular margins observed on the machined surface (figure 2(C), lower left images).

### 3.4. Effects of the nano-topographical surface on human dermal fibroblast cell proliferative activity

Cell viability quantified with WST-1 on the 5 or 10 MAH-treated surfaces was less than 20% of that on the machined surfaces on day 1 ( $p < 0.05$ ; figure 3(A)). The machined surface was still higher in cell number than the 5 or 10 MAH-treated surfaces at day 7 ( $p < 0.05$ ). However, the value on the 5 or 10 MAH-treated surfaces came up to 55% or 70% of that on the machined surface, respectively. There were no significant differences between the surface types in proliferative activity on day 4 ( $p > 0.05$ ; figure 3(B)).

### 3.5. Enhancement of dermal ECM synthesis without a proinflammatory reaction on the nano-topographical surface

Sirius red staining of day 28 cultures demonstrated that collagen deposition increased by 1.2-fold on the 5 MAH-treated surfaces, compared with the machined surfaces (figure 4(A);  $p < 0.05$ ). The 10 MAH-treated surfaces featured the highest collagen deposition, with a value 1.7 times higher than that on the machined surfaces. Dermal matrix gene markers such as *COL1* and 3, *FBN* and *ELN* were consistently upregulated on both the AH-treated titanium surfaces relative to the machined surfaces on day 14 (figure 4(B)). In particular, *COL3* and *FBN1* were substantially expressed on the AH-treated surfaces, in contrast with the low expression on the machined surfaces. There were no significant differences between the surface types in terms of the levels of proinflammatory cytokines such as GM-CSF, IFN- $\gamma$ , IL-1 $\beta$ , -6 and -8, MCP-1 and -3, M-CSF, and TNF- $\alpha$  when measured in surface-bound human dermal fibroblasts on day 1 ( $p > 0.05$ ; figure 4(C)).

### 3.6. Dermal ECM adheres to nano-spikes and infiltrates the nano-pores on the nano-topographical surface

Low-magnification SEM observation of day 28 cultures (figure 5(A),  $\times 250$ ) demonstrated that fibroblastic

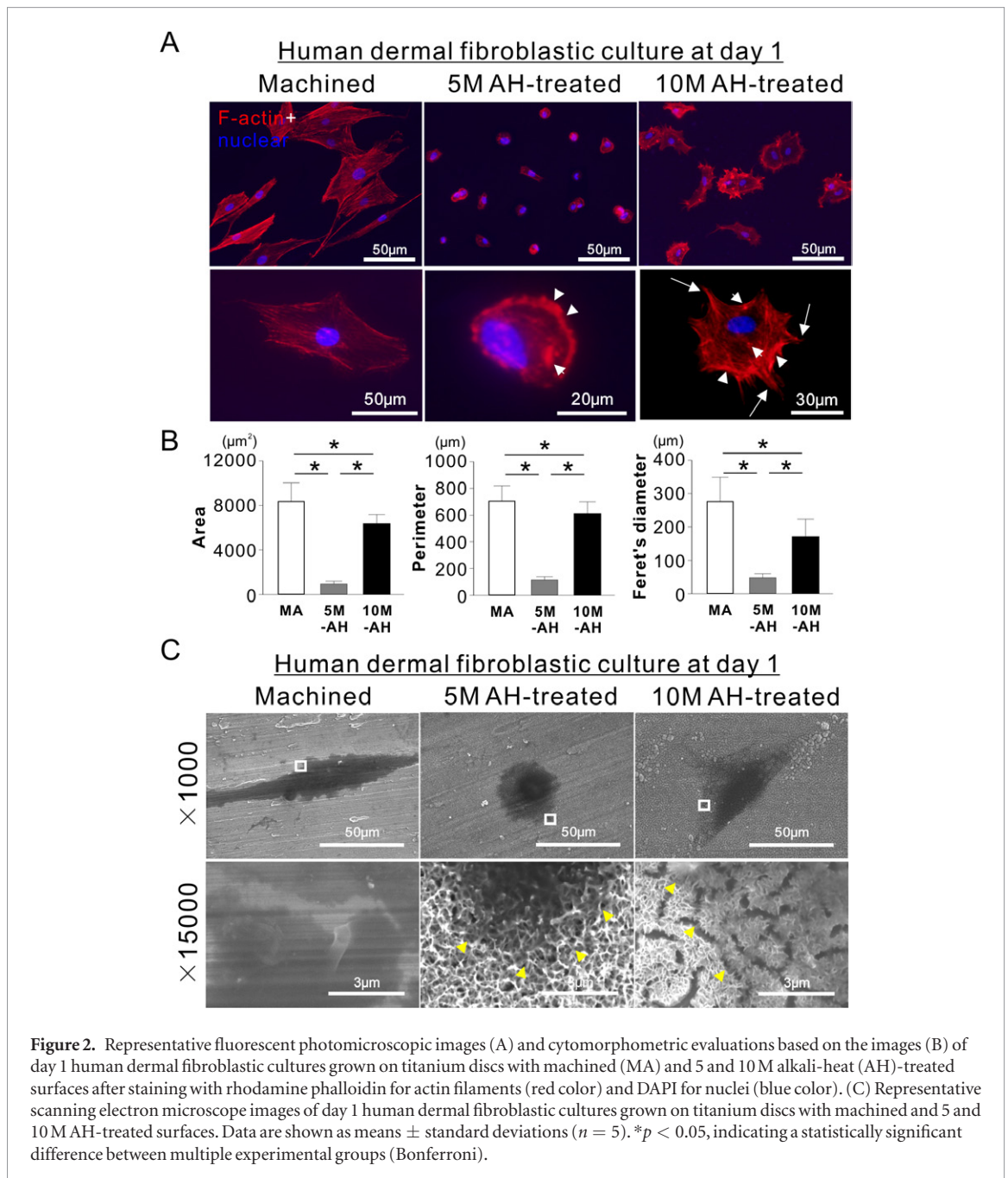


**Figure 2.** Representative fluorescent photomicroscopic images (A) and cytomorphometric evaluations based on the images (B) of day 1 human dermal fibroblastic cultures grown on titanium discs with machined (MA) and 5 and 10 M alkali-heat (AH)-treated surfaces after staining with rhodamine phalloidin for actin filaments (red color) and DAPI for nuclei (blue color). (C) Representative scanning electron microscope images of day 1 human dermal fibroblastic cultures grown on titanium discs with machined and 5 and 10 M AH-treated surfaces. Data are shown as means  $\pm$  standard deviations ( $n = 5$ ). \* $p < 0.05$ , indicating a statistically significant difference between multiple experimental groups (Bonferroni).

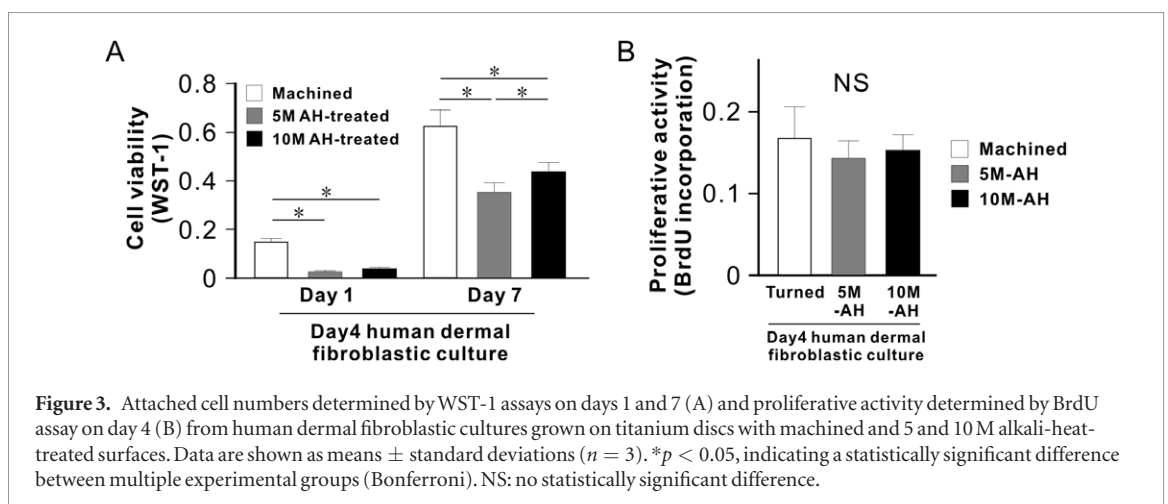
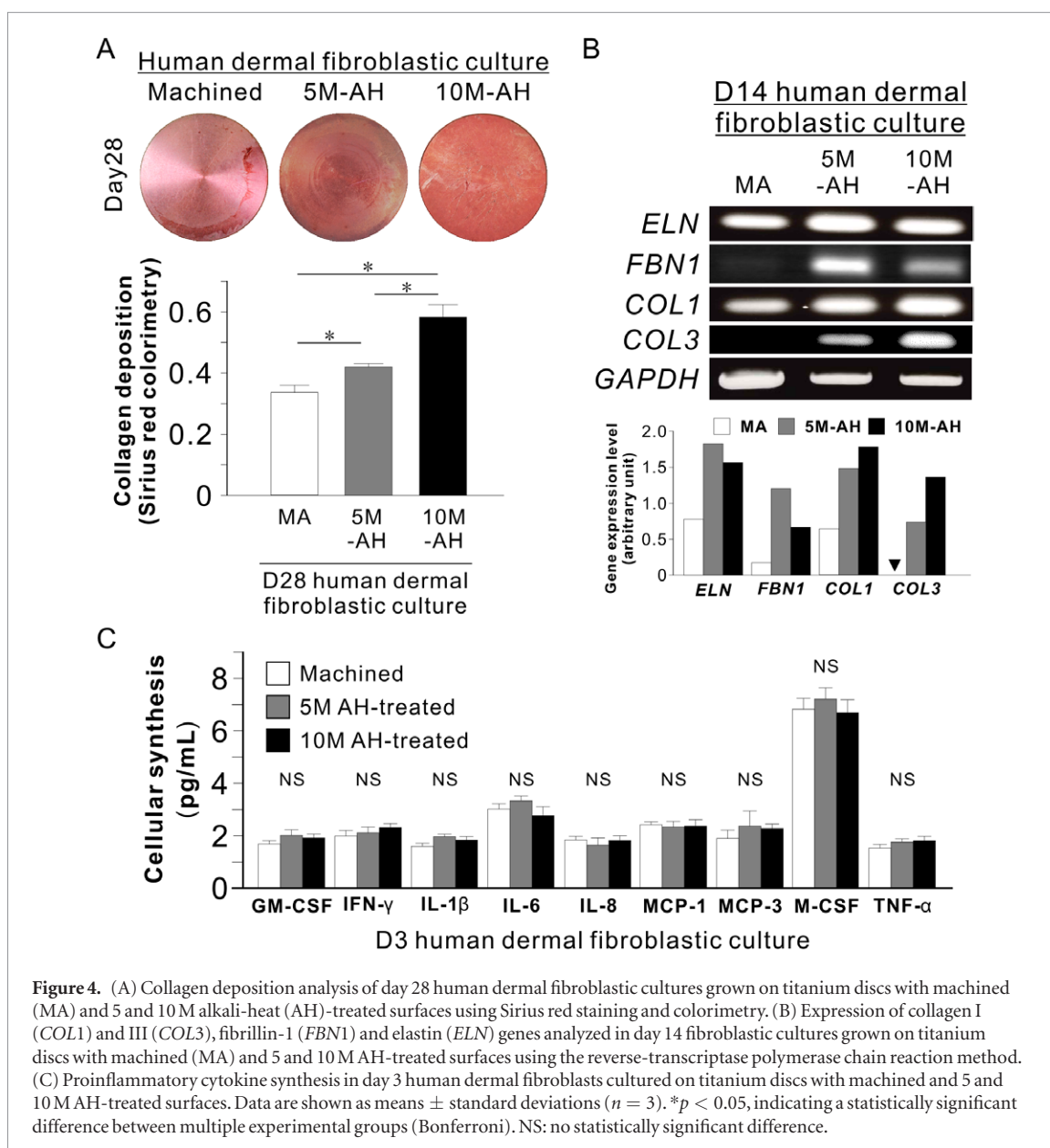


**Figure 3.** Attached cell numbers determined by WST-1 assays on days 1 and 7 (A) and proliferative activity determined by BrdU assay on day 4 (B) from human dermal fibroblastic cultures grown on titanium discs with machined and 5 and 10 M alkali-heat-treated surfaces. Data are shown as means  $\pm$  standard deviations ( $n = 3$ ). \* $p < 0.05$ , indicating a statistically significant difference between multiple experimental groups (Bonferroni). NS: no statistically significant difference.

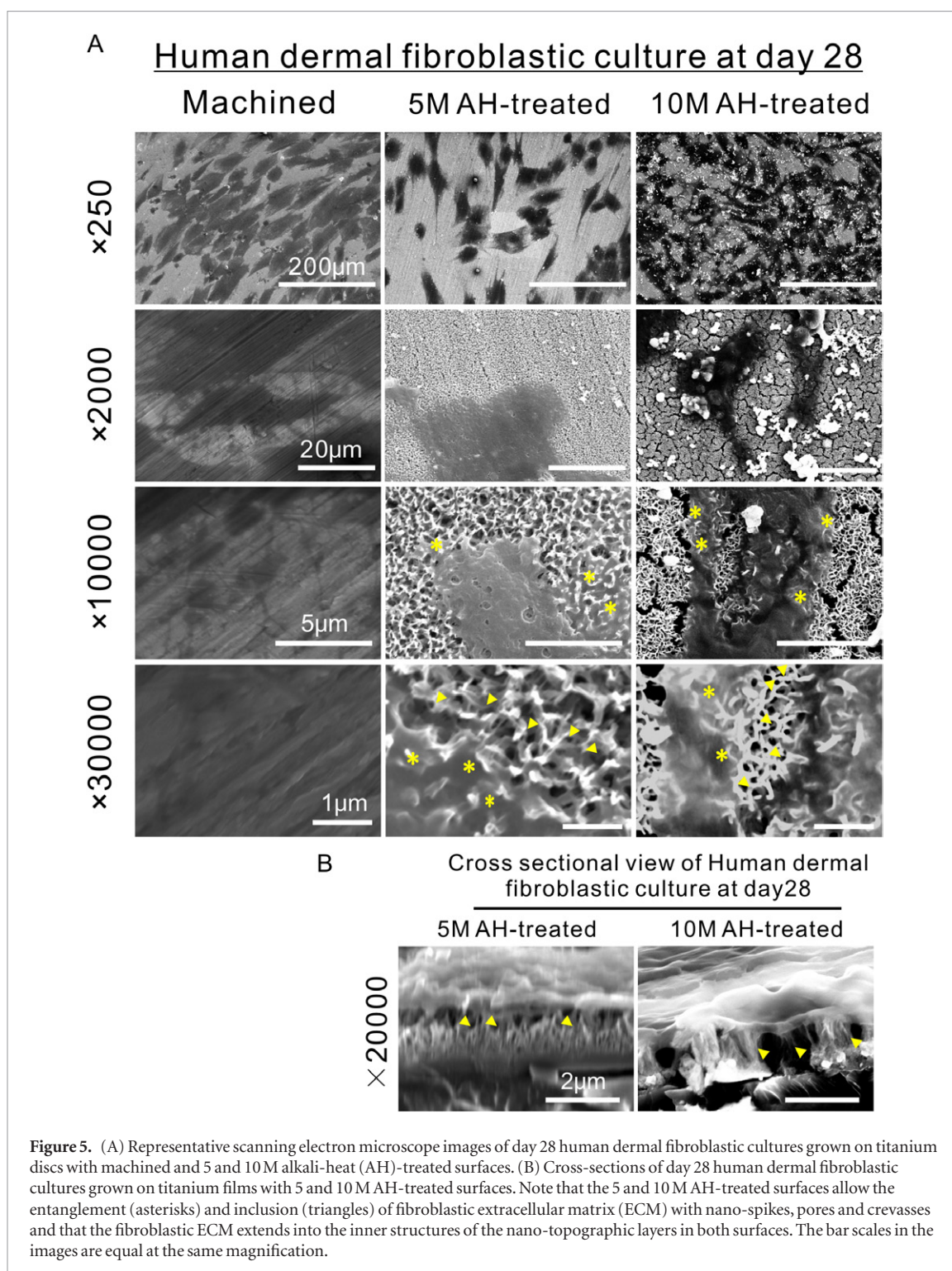


ECM broadly covered both the machined and 10 M AH-treated surfaces, in contrast with the relatively limited deposition on the 5 M AH-treated surface. Mid-range magnification images (figure 5(A),  $\times 2000$ ) indicated that ECM on the machined surface was thin and flat, whereas visually thick and bubbly ECM was observed on both the 5 and 10 M AH-treated surfaces. The ECM margins were tangled in the nano-spikes on both AH-treated surfaces (figure 5(A), asterisks in  $\times 10\,000$  and  $\times 30\,000$  images), in contrast with the spreading edge of ECM on the machined surfaces. High magnification images revealed that the ECM edge appeared to infiltrate the nano-pores on both the 5 and 10 M AH-treated surfaces (figure 5(A), triangles in  $\times 30\,000$  images). SEM observations of cross-sections of day 28 human dermal fibroblast cultures grown on 5 and 10 M AH-treated surfaces (figure 5(B),  $\times 20\,000$ , triangles) demonstrated that the ECM base, which covered the nano-structural layer of the titanium surface, appeared to infiltrate the

nano-structural layer. The ECM borders within the nano-structural layer were unclear and appeared to have been incorporated within the structure.

### 3.7. Sufficient interlocking of human dermal fibroblastic collagen on nano-topographical surfaces to resist mechanical, enzymatic and chemical detachment

At least 30% of the collagen deposited on the 5 and 10 M AH-treated surfaces during a 28 d human fibroblast culture remained after physical detachment (ultrasonic), in contrast with 2% of collagen on the machined surface ( $p < 0.05$ ; figure 6(A)). The 5 and 10 M AH-treated surfaces retained 35% and 45%, respectively, of the collagen deposited during a 28 d culture after exposure to collagenase, which simulated inflammation under culture conditions (figure 6(B)). In contrast, less than 5% of the collagen remained on the machined surface under similar conditions ( $p < 0.05$ ). More than 40% of the collagen deposited on 5 and 10 M



AH-treated surfaces during a 28 d culture remained after exposure to hydrogen peroxide, whereas less than 30% of the collagen remained on the machined surface ( $p < 0.05$ ; figure 6(C)).

SEM observation of the samples after collagenase treatment revealed that the machined surface lost the largest amount of deposited ECM (figure 6(D), left image). In contrast (figure 6(D), middle and right images), the 5 and 10 M AH-treated surfaces retained considerable amounts of deposited collagen even though it was digested by the enzyme treatment (figure 6(D), mid and right images). In particular, the

10 M AH-treated surface remained mostly covered in deposited collagen. On the 5 and 10 M AH-treated surfaces, the detached ends of the ECM appeared as bush-like projections from the surface (figure 6(D), triangles in middle and right images).

#### 4. Discussion

Fibroblasts are not only the principal source of the extensive ECM that is characteristic of skin tissue, but are also central mediators of pathological fibrotic ECM accumulation in response to tissue injury or

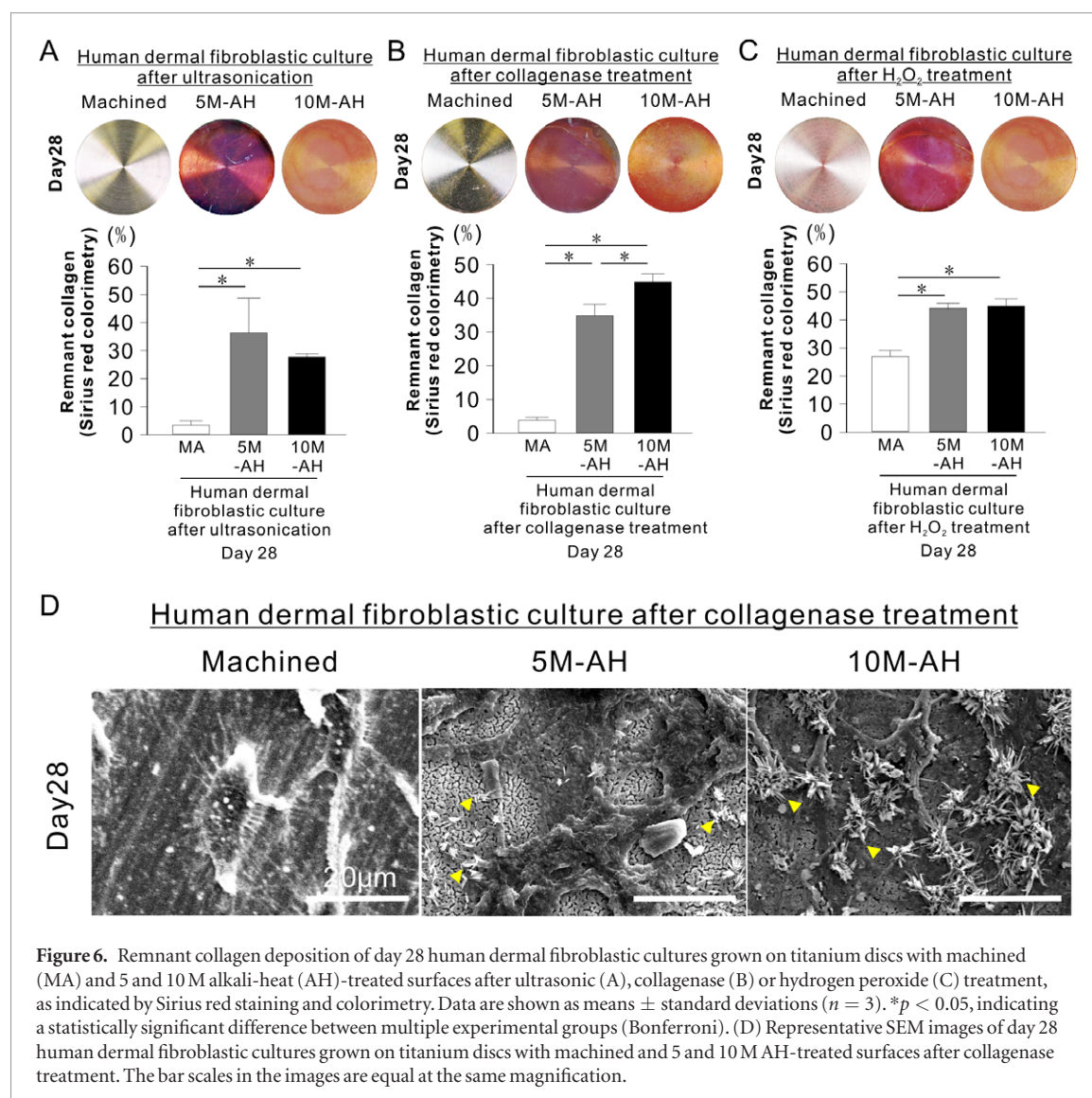


**Figure 6.** Remnant collagen deposition of day 28 human dermal fibroblastic cultures grown on titanium discs with machined (MA) and 5 and 10 M alkali-heat (AH)-treated surfaces after ultrasonic (A), collagenase (B) or hydrogen peroxide (C) treatment, as indicated by Sirius red staining and colorimetry. Data are shown as means  $\pm$  standard deviations ( $n = 3$ ). \* $p < 0.05$ , indicating a statistically significant difference between multiple experimental groups (Bonferroni). (D) Representative SEM images of day 28 human dermal fibroblastic cultures grown on titanium discs with machined and 5 and 10 M AH-treated surfaces after collagenase treatment. The bar scales in the images are equal at the same magnification.

inflammation [25]. The nano-topographic titanium surface induced by AH-treatment enhanced ECM production in human dermal fibroblasts. Both AH-treated surfaces consistently upregulated the gene expression levels of the main dermal connective tissue components such as collagen fibers (type I and III collagen) and elastic fibers (elastin and fibrillin) and induced increased surface collagen deposition. Fluorescent microscopic observation of rhodamine- and DAPI-stained day 1 cultures revealed that similar numbers of cells attached to the AH-treated and machined surfaces. However, the cellular shapes on the AH-treated surfaces were relatively small but exhibited substantial cellular attachment along with the development of focal adhesion and cytoskeletal networks. The nano-topographies of the AH-treated surfaces may therefore support the ability of human dermal fibroblasts to assemble multiple focal adhesions and thus promote dermal fibroblastic ECM production.

Markedly lower cell viability was observed on the AH-treated surfaces, relative to the machined surfaces, on day 1 when measured in WST-1 assay. However, on day 1, WST-1 values of the AH-treated surfaces may

have been affected by differences in the cell shape and surface area, as this reagent detects cellular metabolism throughout the culture [26]. In addition, no significant differences in the human dermal fibroblastic synthesis of representative proinflammatory cytokines were observed among the titanium surface types on day 1. These data suggest that cells attached on the AH-treated surfaces are initially low in cellular metabolism but may fully function during subsequent dermal healing on titanium devices.

Despite differences in the structural densities, the topography of the AH-treated surfaces was characterized by the presence of numerous spikes and pores with a nano-scale 3D internal network. However, AH treatment had little effect on the micro-scale topography of the original machined titanium substrate; this was confirmed by the retention of the original machined grooves, as determined under the SEM, and only small differences in surface roughness parameter at a micron scale on both AH-treated surfaces. Our previous study demonstrated that cellular proliferation and collagen deposition in an oral gingival fibroblastic culture occurred at greater levels on a smooth titanium surface

than on micro-roughened titanium surfaces [27]. The effect of micron-scale titanium surface topography on cellular proliferative activity was previously observed in osteoblastic cells and femoral and jaw periosteal cells [28–30]. On day 4, BrdU incorporation revealed that the proliferative activities of human dermal fibroblasts were not significantly different among the titanium surface types used in the present study. The numbers of cells on the AH-treated surfaces were initially lower, but appeared similar to that on the machined surface at day 7. These data suggested that the influence of micron-level titanium topography on cellular proliferation may be universal and not cell type-specific.

Dermal fibroblasts are normally spindle-shaped and maintain stable adhesions to the substrate via focal adhesions [31]. Focal adhesion consists of transmembrane adhesion molecules binding to ECM and focal adhesion associated protein such as talin and vinculin, which bind to cytoskeleton. The focal adhesion captures and integrates various signals from both the extracellular and intracellular environments [32, 33]. Focal adhesion controls fundamental cellular processes such as differentiation, cell cycle, apoptosis and motility [32, 34], possibly via feedback regulation of the formation of cellular protrusion and the cytoskeletal actin fiber network after initiation of the integrin-mediated cellular signaling pathway [35, 36]. Transmembrane adhesion molecule integrin is approximately 15 nm in size and requires a width of 6 nm to maintain a single adhesion site on a substrate [37]. According to the previous study [9], the estimated diameter of a nano-spike tip on a 5 M or 10 M AH-treated surface was approximately 110 nm or 90 nm, respectively. On nano-topographic substrates, cells tend to form focal adhesions on nano-convex areas, but not concave areas [24]. In the present study, the cells expanded their original shapes on the machined surface. In contrast, on day 1, characteristic morphologies of the attached human dermal fibroblasts were observed on both AH-treated titanium surfaces. Relatively angular or circular cells with spotty accumulations of contractile ring-like structures were observed on the 5 M AH-treated surfaces. In contrast, cells on the 10 M AH-treated surfaces were larger and polytypic (rectangular, spindle or oval shapes), with developed cytoskeletal networks accompanied by actin accumulation within the cell and multiple lamellipodia and filopodia. Filopodia are comprised of parallel actin fibers and serve as sensors with which to explore the environment, whereas lamellipodia are composed of branched actin fibers and are capable of supporting traction forces generated by the actomyosin network, thus inducing unidirectional cellular displacement by pulling the cell body in the direction of the lamellipodia [38]. This finding suggested that dermal fibroblasts on the 10 M AH-treated surface were more motile than those on the 5 M AH-treated surface. This suggestion may explain why in the present study, the 10 M AH-treated surface exhibited greater collagen deposition and deposited ECM coverage (SEM

observation) on day 28 of culture than that by the 5 M AH-treated surface, despite the similarities in proliferation and dermal ECM-related gene expression levels.

The area of deposited ECM in the day 28 culture on the 5 and 10 M AH-treated surface was apparently lower than or comparable with that on the machined surface under SEM observation, respectively. However, the amount of collagen deposition measured by Sirius red was greater on AH-treated surface than on the machined surface. Upregulations of dermal ECM-related genes and the inclusion of ECM into the nano-topographic layer might induce thicker ECM formation on the AH-treated surface than that on the machined surface.

Many studies have investigated the behavior of dermal fibroblasts on micron-to-nano-graded topography. Fibroblasts tend to be directed parallel to lines of unidirectionally aligned collagen nano-fibers or originally-fabricated linear substrate [20, 21]. At the same time, they displayed multiple cellular protrusion with many focal adhesions formed on the originally-fabricated pattern of the substrate [39]. Generally, fibroblasts elongate well on the patterned topography with 500 nm or larger intervals between peaks. In the present study, the median top-to-top distances were approximately 300 nm or 200 nm on the 5 M or 10 M AH-treated surface, respectively. This may explain the characteristic cellular morphology observed on these surfaces in the present study. Moreover, many reports have stated that polymer scaffolds with anisotropically-patterned nano-topographies could determine the fate and differentiation of various types of cells such as neural progenitor cells [40–43], neural stem cells [44], embryonic stem cells [45] and mesenchymal stem cells [46]. All of those substrates featured relatively micron-to-submicron pitches ranging from 500 nm to several  $\mu\text{m}$ . In the present study, the array of nano-spikes and pores on the 10 M AH-treated surfaces were anisotropically-patterned and random topography, in contrast with the relatively isotropically-patterned appearance on the 5 M AH-treated surfaces. An investigation of the cellular responses of other mesenchymal or stem cells to these AH-treated titanium surfaces in association with the determination of more detailed nano-topography would be of great interest in the future.

Our previous study demonstrated that the AH-treated nano-topographical titanium surface promoted the inclusion of gingival fibroblastic collagen fiber into the surface both *in vitro* and *in vivo* [9]. This was determined by SEM observation, ECM detachment assays, and elemental analyses of superficial and cross-sectional specimens of the deposited ECM on the AH-treated (particularly the 10 M AH-treated) titanium surfaces. In day 28 cultures of human dermal fibroblasts in the present study, the deposited ECM margins buried with the nano-spikes and infiltrated the nano-pores on both AH-treated surfaces. Cross-sectional specimens of day 28 cultures confirmed that the ECM deposited on the AH-treated surfaces had

infiltrated the superficial nano-topographic layers. The dermal ECM deposited on the AH-treated surfaces was strongly resistant to detachment treatments intended to experimentally mimic mechanical force or tissue inflammation. All of these results were nearly identical to those obtained in a previous gingival connective tissue model study [9]. That study also demonstrated the surface inclusion of gingival connective tissue and gingival collagen fiber orientation perpendicular to the 10 M AH-treated titanium implant surface in a rabbit gingival model; notably, these outcomes were never observed on the machined implant surface.

The inclusion of collagen fibers in nano-pores likely requires the infiltration of cell bodies or protrusion. Both the previous [9] and present studies demonstrate that nano-sized pores of the superficial topographic layer allowed gingival and dermal fibroblastic ECM to infiltrate it on both types of AH-treated titanium surfaces. On a polyethylene glycol linear substrate, cells may completely infiltrate pores with 800 nm grooves but only partially infiltrate 400 nm grooves [47]. Our previous study of the same surfaces revealed nano-pores measuring 100 nm and 200 nm in diameter on the 5 M and 10 M AH-treated surfaces, respectively [9]. Increase of calcium accumulation was observed on both AH-treated surfaces after a 7 d immersion in culture media, but not on the machined titanium surface. This corresponded to the previous observation of calcium phosphate apatite formation on an AH-treated surface after immersion in a simulated body fluid [48–50]. In fact, AH treatment changed the surface chemical composition of titanium to sodium titanate; this theoretically contributed to apatite nucleation via the exchange of sodium ions with calcium ions [50]. Accumulated calcium ions electrostatically serve as a divalent cation bridge between the substrate and negatively charged proteins containing the RGD (arginine-glycine-aspartate) motif [51]. In the present study, this specific chemical property of the AH-treated surface helped dermal fibroblasts to progressively infiltrate or to protrude into the nano-sized pores.

AH treatment can be applied to various forms of titanium and titanium alloys. In fact, the previous [9] and present studies confirmed that use of the same AH method could produce the same nano-topography on grade I titanium film, grade II titanium discs and screw implants. This indicates the universal applicability of this AH treatment method for titanium-based percutaneous devices and titanium components of percutaneous polymer-based devices. An investigation of the sealing effects and histological features of these AH-treated nano-topographical titanium surfaces on percutaneous medical devices in pre-clinical animal models would be intriguing.

## 5. Conclusion

AH treatment creates nano-topographic titanium surfaces with well-organized nano-spikes and pores

that form isotropically- or anisotropically-patterned arrays. These surfaces were found to enhance human dermal fibroblastic ECM synthesis without inducing a proinflammatory reaction or proliferation and to establish a sufficient mechanical integration between the ECM and surface to resist mechanical, enzymatic and chemical detachment treatments intended to experimentally mimic overloading and inflammatory conditions.

## Acknowledgment

The author would like to thank research associate E Watanabe of the Oral Health Science Center for her assistance with the evaluation of chemical composition by EPMA. This research was supported by Grant-in-Aid for Scientific Research (C) of Japan, 2014–2016 (grant number 26462978).

## References

- [1] Affeld K, Grosshauser J, Goubergrits L and Kertzscher U 2012 Percutaneous devices: a review of applications, problems and possible solutions *Expert Rev. Med. Devices* **9** 389–99
- [2] Lyon C C, Kulkarni J, Zimerson E, Van Ross E and Beck M H 2000 Skin disorders in amputees *J. Am. Acad. Dermatol.* **42** 501–7
- [3] Tillander J, Hagberg K, Hagberg L and Branemark R 2010 Osseointegrated titanium implants for limb prostheses attachments: infectious complications *Clin. Orthop. Relat. Res.* **468** 2781–8
- [4] Carlsson L, Rostlund T, Albrektsson B, Albrektsson T and Branemark P I 1986 Osseointegration of titanium implants *Acta Orthop. Scand.* **57** 285–9
- [5] Abarrategi A *et al* 2008 Multiwall carbon nanotube scaffolds for tissue engineering purposes *Biomaterials* **29** 94–102
- [6] Usui Y *et al* 2008 Carbon nanotubes with high bone-tissue compatibility and bone-formation acceleration effects *Small* **4** 240–6
- [7] Ueno T, Tsukimura N, Yamada M and Ogawa T 2011 Enhanced bone-integration capability of alkali- and heat-treated nanopolymorphic titanium in micro-to-nanoscale hierarchy *Biomaterials* **32** 7297–308
- [8] Nishio K *et al* 2000 The effect of alkali- and heat-treated titanium and apatite-formed titanium on osteoblastic differentiation of bone marrow cells *J. Biomed. Mater. Res.* **52** 652–61
- [9] Kato E, Sakurai K and Yamada M 2015 Periodontal-like gingival connective tissue attachment on titanium surface with nano-ordered spikes and pores created by alkali-heat treatment *Dent. Mater.* **31** e116–30
- [10] Kubo K *et al* 2009 Cellular behavior on TiO<sub>2</sub> nanonodular structures in a micro-to-nanoscale hierarchy model *Biomaterials* **30** 5319–29
- [11] Raimondo T, Puckett S and Webster T J 2010 Greater osteoblast and endothelial cell adhesion on nanostructured polyethylene and titanium *Int. J. Nanomed.* **5** 647–52
- [12] Yao C, Slamovich E B and Webster T J 2008 Enhanced osteoblast functions on anodized titanium with nanotube-like structures *J. Biomed. Mater. Res. A* **85** 157–66
- [13] Ballo A, Agheli H, Lausmaa J, Thomsen P and Petronis S 2011 Nanostructured model implants for *in vivo* studies: influence of well-defined nanotopography on *de novo* bone formation on titanium implants *Int. J. Nanomed.* **6** 3415–28
- [14] Mendonca G, Mendonca D B, Aragao F J and Cooper L F 2008 Advancing dental implant surface technology—from micron—to nanotopography *Biomaterials* **29** 3822–35

- [15] Divya Rani V V, Manzoor K, Menon D, Selvamurugan N and Nair SV 2009 The design of novel nanostructures on titanium by solution chemistry for an improved osteoblast response *Nanotechnology* **20** 195101
- [16] Cooper L F *et al* 2006 Fluoride modification effects on osteoblast behavior and bone formation at TiO<sub>2</sub> grit-blasted c.p. titanium endosseous implants *Biomaterials* **27** 926–36
- [17] Ellingsen J E, Johansson C B, Wennerberg A and Holmen A 2004 Improved retention and bone-to-implant contact with fluoride-modified titanium implants *Int. J. Oral Maxillofac. Implants* **19** 659–66 (PMID: 15508981)
- [18] Mathieu P S and Lobo A G 2012 Cytoskeletal and focal adhesion influences on mesenchymal stem cell shape, mechanical properties, and differentiation down osteogenic, adipogenic, and chondrogenic pathways *Tissue Eng. B* **18** 436–44
- [19] Salasznyk R M, Klees R F, Williams W A, Boskey A and Plopper G E 2007 Focal adhesion kinase signaling pathways regulate the osteogenic differentiation of human mesenchymal stem cells *Exp. Cell Res.* **313** 22–37
- [20] Biela S A, Su Y, Spatz J P and Kemkemer R 2009 Different sensitivity of human endothelial cells, smooth muscle cells and fibroblasts to topography in the nano-micro range *Acta Biomater.* **5** 2460–6
- [21] Muthusubramaniam L, Zaitseva T, Paukshto M, Martin G and Desai T 2014 Effect of collagen nanotopography on keloid fibroblast proliferation and matrix synthesis: implications for dermal wound healing *Tissue Eng. A* **20** 2728–36
- [22] Palaiologou A A, Yukna R A, Moses R and Lallier T E 2001 Gingival, dermal, and periodontal ligament fibroblasts express different extracellular matrix receptors *J. Periodontol.* **72** 798–807
- [23] Guo F, Carter D E, Mukhopadhyay A and Leask A 2011 Gingival fibroblasts display reduced adhesion and spreading on extracellular matrix: a possible basis for scarless tissue repair? *PLoS One* **6** e27097
- [24] Kim D H, Han K, Gupta K, Kwon K W, Suh K Y and Levchenko A 2009 Mechanosensitivity of fibroblast cell shape and movement to anisotropic substratum topography gradients *Biomaterials* **30** 5433–44
- [25] Kendall R T and Feghali-Bostwick C A 2014 Fibroblasts in fibrosis: novel roles and mediators *Front. Pharmacol.* **5** 123
- [26] Yin L M, Wei Y, Wang Y, Xu Y D and Yang Y Q 2013 Long term and standard incubations of WST-1 reagent reflect the same inhibitory trend of cell viability in rat airway smooth muscle cells *Int. J. Med. Sci.* **10** 68–72
- [27] Att W, Yamada M and Ogawa T 2009 Effect of titanium surface characteristics on the behavior and function of oral fibroblasts *Int. J. Oral Maxillofac. Implants* **24** 419–31 (PMID: 19587863)
- [28] Takeuchi K, Saruwatari L, Nakamura H K, Yang J M and Ogawa T 2005 Enhanced intrinsic biomechanical properties of osteoblastic mineralized tissue on roughened titanium surface *J. Biomed. Mater. Res. A* **72** 296–305
- [29] Kubo K *et al* 2008 Microtopography of titanium suppresses osteoblastic differentiation but enhances chondroblastic differentiation of rat femoral periosteum-derived cells *J. Biomed. Mater. Res. A* **87** 380–91
- [30] Att W, Kubo K, Yamada M, Maeda H and Ogawa T 2009 Biomechanical properties of jaw periosteum-derived mineralized culture on different titanium topography *Int. J. Oral Maxillofac. Implants* **24** 831–41 (PMID: 19865623)
- [31] Cai Y and Sheetz M P 2009 Force propagation across cells: mechanical coherence of dynamic cytoskeletons *Curr. Opin. Cell Biol.* **21** 47–50
- [32] Ruoslahti E and Obrink B 1996 Common principles in cell adhesion *Exp. Cell Res.* **227** 1–11
- [33] Rosales C, O'Brien V, Kornberg L and Juliano R 1995 Signal transduction by cell adhesion receptors *Biochim. Biophys. Acta* **1242** 77–98 (PMID: 7542926)
- [34] Huang S and Ingber D E 2000 Shape-dependent control of cell growth, differentiation, and apoptosis: switching between attractors in cell regulatory networks *Exp. Cell Res.* **261** 91–103
- [35] Tang D D and Anfnigenova Y 2008 Physiologic properties and regulation of the actin cytoskeleton in vascular smooth muscle *J. Cardiovasc. Pharmacol. Ther.* **13** 130–40
- [36] Chen G C, Turano B, Ruest P J, Hagel M, Settleman J and Thomas S M 2005 Regulation of Rho and Rac signaling to the actin cytoskeleton by paxillin during *Drosophila* development *Mol. Cell Biol.* **25** 979–87
- [37] Kim D H, Lee H, Lee Y K, Nam J M and Levchenko A 2010 Biomimetic nanopatterns as enabling tools for analysis and control of live cells *Adv. Mater.* **22** 4551–66
- [38] Hanein D and Horwitz A R 2012 The structure of cell-matrix adhesions: the new frontier *Curr. Opin. Cell Biol.* **24** 134–40
- [39] Kim D H, Seo C H, Han K, Kwon K W, Levchenko A and Suh K Y 2009 Guided cell migration on microtextured substrates with variable local density and anisotropy *Adv. Funct. Mater.* **19** 1579–86
- [40] Marino A *et al* 2013 Two-photon polymerization of sub-micrometric patterned surfaces: investigation of cell-substrate interactions and improved differentiation of neuron-like cells *ACS Appl. Mater. Interfaces* **5** 13012–21
- [41] Chua J S *et al* 2014 Extending neurites sense the depth of the underlying topography during neuronal differentiation and contact guidance *Biomaterials* **35** 7750–61
- [42] Wang P Y, Li W T, Yu J and Tsai W B 2012 Modulation of osteogenic, adipogenic and myogenic differentiation of mesenchymal stem cells by submicron grooved topography *J. Mater. Sci. Mater. Med.* **23** 3015–28
- [43] Tan K K *et al* 2015 Enhanced differentiation of neural progenitor cells into neurons of the mesencephalic dopaminergic subtype on topographical patterns *Biomaterials* **43** 32–43
- [44] Yang K *et al* 2014 Multiscale, hierarchically patterned topography for directing human neural stem cells into functional neurons *ACS Nano* **8** 7809–22
- [45] Ankam S, Lim C K and Yim E K 2015 Actomyosin contractility plays a role in MAP2 expression during nanotopography-directed neuronal differentiation of human embryonic stem cells *Biomaterials* **47** 20–8
- [46] Wu Y N *et al* 2014 Substrate topography determines the fate of chondrogenesis from human mesenchymal stem cells resulting in specific cartilage phenotype formation *Nanomed.: Nanotechnol. Biol. Med.* **10** 1507–16
- [47] Kim D H *et al* 2010 Nanoscale cues regulate the structure and function of macroscopic cardiac tissue constructs *Proc. Natl Acad. Sci. USA* **107** 565–70
- [48] Janson I A, Kong Y P and Putnam A J 2014 Nanotopographic substrates of poly (methyl methacrylate) do not strongly influence the osteogenic phenotype of mesenchymal stem cells *in vitro* *PLoS One* **9** e90719
- [49] Miyaza T, Kim H M, Kokubo T, Ohtsuki C, Kato H and Nakamura T 2002 Mechanism of bonelike apatite formation on bioactive tantalum metal in a simulated body fluid *Biomaterials* **23** 827–32
- [50] Kim H M, Miyaji F, Kokubo T and Nakamura T 1996 Preparation of bioactive Ti and its alloys via simple chemical surface treatment *J. Biomed. Mater. Res.* **32** 409–17
- [51] Takeichi M and Okada T S 1972 Roles of magnesium and calcium ions in cell-to-substrate adhesion *Exp. Cell Res.* **74** 51–60